Imaging Neuroscience
an open access journal

Research Article

Frame-wise multi-echo distortion correction for superior functional MRI

Andrew N. Van[a,b], David F. Montez[b,c], Timothy O. Laumann[c], Philip N. Cho[b], Vahdeta Suljic[b], Thomas Madison[d,e], Noah J. Baden[b], Nadeshka Ramirez-Perez[b], Kristen M. Scheidter[b], Julia S. Monk[b], Forrest I. Whiting[b], Babatunde Adeyemo[b], Roselyne J. Chauvin[b], Samuel R. Krimmel[b], Athanasia Metoki[b], Aishwarya Rajesh[f], Jarod L. Roland[g], Taylor Salo[h], Anxu Wang[b,i], Kimberly B. Weldon[e], Aristeidis Sotiras[f,j], Joshua S. Shimony[f], Benjamin P. Kay[b], Steven M. Nelson[e,k], Brenden Tervo-Clemmens[e,l], Scott A. Marek[f], Luca Vizioli[m], Essa Yacoub[m], Theodore D. Satterthwaite[h], Evan M. Gordon[f], Damien A. Fair[d,e,k], M. Dylan Tisdall[n], Nico U.F. Dosenbach[a,b,f,o]

[a]Department of Biomedical Engineering, Washington University in St. Louis, St. Louis, MO, United States
[b]Department of Neurology, Washington University School of Medicine, St. Louis, MO, United States
[c]Department of Psychiatry, Washington University School of Medicine, St. Louis, MO, United States
[d]Institute of Child Development, University of Minnesota Medical School, Minneapolis, MN, United States
[e]Masonic Institute for the Developing Brain, University of Minnesota Medical School, Minneapolis, MN, United States
[f]Department of Radiology, Washington University School of Medicine, St. Louis, MO, United States
[g]Department of Neurosurgery, Washington University School of Medicine, St. Louis, MO, United States
[h]Lifespan Informatics and Neuroimaging Center (PennLINC), Perelman School of Medicine, University of Pennsylvania, Philadelphia, PA, United States
[i]Division of Computation and Data Science, Washington University School of Medicine, St. Louis, MO, United States
[j]Institute for Informatics, Data Science & Biostatistics, Washington University School of Medicine, St. Louis, MO, United States
[k]Department of Pediatrics, University of Minnesota Medical School, Minneapolis, MN, United States
[l]Department of Psychiatry & Behavioral Sciences, University of Minnesota Medical School, Minneapolis, MN, United States
[m]Center for Magnetic Resonance Research, University of Minnesota Medical School, Minneapolis, MN, United States
[n]Department of Radiology, Perelman School of Medicine, University of Pennsylvania, Philadelphia, PA, United States
[o]Department of Pediatrics, Washington University School of Medicine, St. Louis, MO, United States

Corresponding Authors: Andrew N. Van (vanandrew77@gmail.com), Philip N. Cho (c.philip@wustl.edu)

ABSTRACT

Functional MRI (fMRI) data are severely distorted by magnetic field (B0) inhomogeneities, which currently must be corrected using separately acquired field map data. However, changes in the head position of a participant across fMRI frames cause changes in the B0 field, preventing accurate correction of geometric distortions. Movement during field map acquisitions corrupts field maps, preventing distortion correction altogether. In this study, we use multi-echo (ME) fMRI data to dynamically sample and correct for magnetic field image distortions caused by head motion. Our distortion correction pipeline, MEDIC (Multi-Echo DIstortion Correction), leverages magnetic field inhomogeneity information found in the difference between echoes and uses it to correct for distortion on a frame-by-frame basis. Here, we demonstrate that MEDIC's frame-wise distortion correction decreases the impact of head motion on resting-state functional connectivity (RSFC) maps and improves alignment to anatomy when compared with the prior gold standard approach (i.e., FSL TOPUP). Enhanced frame-wise distortion correction with MEDIC, without the requirement for field map collection, furthers the benefit of cutting-edge multi-echo fMRI imaging over single-echo fMRI.

Keywords: distortion correction, fMRI, multi-echo

Received: 22 January 2024 Revision: 22 April 2026 Accepted: 22 April 2026 Available Online: 12 May 2026

The MIT Press

Imaging Neuroscience, Volume 4, 2026
https://doi.org/10.1162/IMAG.a.1262

1. INTRODUCTION

Functional MRI (fMRI) data acquired using echo planar imaging (EPI) sequences are prone to local image distortions due to magnetic field inhomogeneities (B0) arising from differences in magnetic susceptibility, particularly across air–tissue interfaces (Haskell et al., 2023). The orbitofrontal and inferior temporal cortices suffer the largest distortion due to their proximity to the sinuses, mastoids, and ear canals (Brown et al., 2014), but distortion is present to varying degrees across the brain. The presence of local image distortion is particularly problematic for functional connectivity (FC) and task fMRI analyses, which rely on accurate co-registration of functional and anatomical data. Image distortion degrades the performance of registration algorithms used to align functional data to anatomical data and prevents accurate spatial localization of anatomical features in fMRI studies (Cusack et al., 2003; Togo et al., 2017).

To correct geometric distortions in fMRI data, dedicated field map scans are acquired before or after fMRI acquisitions to estimate the B0 field inhomogeneity (Andersson et al., 2003; Jezzard & Balaban, 1995). However, such static distortion correction approaches are vulnerable to head motion (Andersson et al., 2018) and represent only a snapshot of the field inhomogeneities. Head movement during fMRI is notorious for introducing significant noise and systematic artifacts into the data (Power et al., 2012), and in the context of susceptibility artifact correction, head motion compromises the accuracy of field map data. Because head rotations about axes orthogonal to the main magnetic field (i.e., through-plane rotations, when slices are defined axially) change the susceptibility-induced inhomogeneities in the B0 magnetic field (Graham et al., 2017), distortion corrections estimated from separately collected field maps are accurate only so long as the participant's head remains in the same position as during field map collection. Furthermore, head movements during the field map acquisition itself, as well as misregistration errors between the field map and fMRI data, can introduce additional errors that limit the utility of static distortion correction.

A handful of dynamic distortion correction methods have been developed to address time-varying changes in distortion (Hutton et al., 2013; Visser et al., 2012; Wilm et al., 2011), which have repeatedly demonstrated effectiveness. However, many of these methods are challenging to implement due to a need for additional hardware or a lack of available open-source software. Some methods also continue to require the acquisition of a static field map, making these methods vulnerable to the same field map errors described previously. Thus, an easily integrated distortion correction method that is robust to head motion and position would greatly benefit fMRI, particularly where motion may be related to phenomena of interest (Makowski et al., 2019).

Multi-echo fMRI (ME-fMRI) has been shown to have several advantages for Blood Oxygen Level Dependent (BOLD) signal detection relative to single-echo sequences (Kundu et al., 2012). By combining data across echoes, ME-fMRI increases BOLD signal sensitivity, particularly to regions that have significant signal dropout at typical single-echo times (Posse, 2012). Further, multiple echo times allow modeling and separation of neurobiologically relevant fMRI signals from physiological and physics-related artifacts (Kundu et al., 2013, 2017). These features of ME-fMRI have been shown to improve reliability of RSFC estimation, especially in clinically relevant subcortical brain regions such as the subgenual cingulate, basal ganglia, and cerebellum (Lynch et al., 2020). The improved reliability is attributed to greater signal-to-noise ratio (SNR), enabling more rapid and precise mapping of the brain.

fMRI data are complex signals composed of magnitude and phase components, where magnitude images at each repetition time (TR) are typically used to evaluate temporal changes in BOLD contrast via T2*. However, ME-fMRI phase data from each TR provide spatial and temporal information about magnetic field variations. By measuring the difference in phase between echoes in ME-fMRI data, the B0 field inhomogeneity can be estimated as the slope of the linear relationship between phase and echo time (Jezzard & Balaban, 1995). Since phase information can be acquired at every TR, a frame-by-frame measure of the B0 field inhomogeneity can be estimated, allowing for more accurate, motion-robust, frame-wise correction of susceptibility distortion in ME-fMRI data. Frame-wise distortion correction in ME-fMRI also eliminates the need for separate field map acquisitions, which are required for static distortion correction.

Capitalizing on the recent surge in ME-fMRI usage, we built an easy-to-use, precise processing pipeline for dynamic, frame-wise distortion correction. Here we describe our open-source, high-speed Multi-Echo DIstortion Correction (MEDIC) algorithm for correcting susceptibility distortions in fMRI data. Comparisons of MEDIC against a current gold standard method, which uses a single static B0 estimation and correction (TOPUP) (Andersson et al., 2003), demonstrate its superiority, especially in the presence of head motion.

2. METHODS

2.1. Multi-echo distortion correction (MEDIC)

To obtain field maps at each frame of an ME-fMRI acquisition, phase at multiple echo times must be measured.

The field map is the slope of the relationship between phase and echo time. Therefore, at a minimum, at least two echoes are needed to compute the phase accumulation over time, that is, the field map.

Computing the field map is complicated by several factors. First, the phase measured at each echo time contains a constant offset, such that the phase at zero echo time is not zero. This is a result of the coil combination process during reconstruction of the phase images, which can result in a phase offset (Eckstein et al., 2018). The second is the wrapping of the phase measurements, which bounds the domain of the measured phase between $[-\pi, \pi]$ (Dymerska et al., 2021). This is a result of the phase being a periodic function and is a common problem when measuring a signal's phase information. Finally, the measured field map obtained from an ME-fMRI image is in the space of the distorted image, and must be transformed to the undistorted space to be used for distortion correction.

2.1.1. The wrapped phase difference problem

Consider a single frame of ME-fMRI data, where n echoes of phase and magnitude data are acquired at different echo times $t_1, t_2, \ldots, t_n$. Using the phase difference method (Dymerska et al., 2021; Jezzard & Balaban, 1995), the phase information of the ME-EPI data can be related to the B0 field inhomogeneity by the following:

$$\Delta\phi = \gamma \Delta B_0 \Delta t, \tag{1}$$

where $\Delta\phi$ is the phase difference between two echoes, γ is the gyromagnetic ratio, ΔB_0 is the B0 field inhomogeneity, and t is the echo time difference. For brevity, we denote the field map as f, which is defined as $f = \gamma \Delta B_0$. When images acquired from more than two echoes are available, Eq. (1) generalizes to

$$\begin{bmatrix} \phi_1(\vec{r}) \\ \phi_2(\vec{r}) \\ \vdots \\ \phi_n(\vec{r}) \end{bmatrix} = f(\vec{r}) \begin{bmatrix} t_1 \\ t_2 \\ \vdots \\ t_n \end{bmatrix}, \tag{2}$$

where $\vec{r}$ is the spatial location for a given voxel, and n denotes the number of echoes in the data. Solving Eq. (2) for f amounts to solving N linear systems, where N is the number of voxels in the image.

In practice, solving Eq. (2) is complicated by two additional effects. The first is that phase information acquired from the scanner is wrapped, such that phase values beyond the range of $[-\pi, \pi]$, are wrapped back into the other side of the interval. The second is that Eq. (2) assumes that the phase accumulation at t=0 is zero, a fact that, depending on the specifics of the coil-combine algorithm applied to the phase data, is often not the case. The full model accounting for both of these effects is given by

$$\begin{bmatrix} \left(\Omega\left(\phi_1(\vec{r})\right)\right)^u \\ \left(\Omega\left(\phi_2(\vec{r})\right)\right)^u \\ \vdots \\ \left(\Omega\left(\phi_n(\vec{r})\right)\right)^u \end{bmatrix} = f(\vec{r}) \begin{bmatrix} t_1 \\ t_2 \\ \vdots \\ t_n \end{bmatrix} + \phi_0(\vec{r}), \tag{3}$$

where Ω is a wrapping operator, such that $\phi_n^{wrapped} = \Omega(\phi_n)$, the wrapped phase, and $(\cdot)^u$ is an unwrapping operator, such that $\phi_n = \left(\Omega(\phi_n)\right)^u = \phi_n^{wrapped} + 2\pi k$ for some integer k, and ϕ_0 is the phase accumulation at $t = 0$. Note that the wrapped phase $\phi_n^{wrapped}$ is what is measured off the scanner. With the addition of phase wrapping and offset effects, Eq. (3) is no longer a simple linear system when trying to solve for f.

2.1.2. Phase offset correction and unwrapping

Estimation and removal of the phase offset are accomplished using the MCPC-3D-S algorithm (Eckstein et al., 2018). MCPC-3D-S estimates the phase offset by computing the unwrapped phase difference between the first and second echoes of the data, then estimating the phase offset by assuming linear phase accumulation between the first and second echoes. This is given by the following:

$$\phi_0(\vec{r}) = \Omega\left(\phi_1(\vec{r})\right) - \left(\frac{t_1}{t_2 - t_1}\right)\left(\Omega\left(\phi_2(\vec{r})\right) - \Omega\left(\phi_1(\vec{r})\right)\right)^u \bmod 2\pi. \tag{4}$$

In the case of MCPC-3D-S, the ROMEO unwrapping algorithm is used to unwrap $\left(\Omega\left(\phi_2(\vec{r})\right) - \Omega\left(\phi_1(\vec{r})\right)\right)$ (Dymerska et al., 2021). Once ϕ_0 is computed, the effects of the phase offset can be removed from Eq. (3) by subtracting ϕ_0 from the phase at each echo time.

Phase unwrapping is performed using the ROMEO algorithm (Dymerska et al., 2021). Phase information at later echoes tends to suffer from phase wrapping more than phase information at earlier echoes due to larger amounts of phase accumulation. This can degrade the performance of phase unwrapping algorithms that only consider the phase unwrapping problem at each echo time independently. ROMEO is able to constrain the unwrapping solution across all echoes by modeling the linear phase accumulation across echoes. This provides more accurate phase unwrapping solutions over other phase unwrapping methods, but requires the removal of phase offsets prior to unwrapping. The unwrapped outputs are then processed further by MEDIC to implement steps not found in the standard ROMEO toolbox, such as low rank approximation (see below).

2.1.3. Temporal phase correction

In a small minority of frames, the phase unwrapping algorithm described above can arrive at a solution that differs from the true phase accumulation by a multiple of 2π, introducing large discontinuities in the time series. To ensure phase unwrapping consistency across frames, once the phases of all frames in a single ME-fMRI scan are unwrapped, a temporal correction step is applied. For each frame, the phase of the first echo is considered against every other frame in an ME-fMRI scan that has a similar correlation with their corresponding magnitude image. Within a group of frames with a correlational similarity of 0.98 or greater, the phase values are corrected by adding/subtracting the nearest 2π multiple that minimizes the difference to the mean phase value of the group, given by

$$\phi_{m,1}^{offset}\left(\vec{r}\right) = 2\pi \cdot \left\lfloor \frac{\overline{\phi_{m,1}}\left(\vec{r}\right) - \phi_{m,1}}{2\pi} \right\rceil, \tag{5}$$

where m denotes the frame index of the EPI time series, $\lfloor \rceil$ denotes the rounding operator, and $\overline{\phi_{m,1}}\left(\vec{r}\right)$ is the mean phase value for the grouped first echo frames similar to frame m. Temporal phase correction for subsequent echoes is performed by linearly projecting the expected phase values beyond the previous echoes:

$$\phi_{m,n}^{offset}\left(\vec{r}\right) = 2\pi \cdot \left\lfloor \frac{1}{2\pi} \cdot \left(\phi_{m,n}\left(\vec{r}\right) - t_n \cdot \sum_{i=1}^{n-1} \frac{\phi_{m,i}\left(\vec{r}\right) t_i}{\sum_{j=1}^{n-1} t_j^2} \right) \right\rceil, \tag{6}$$

where n denotes the index of any echo after the first echo, and t is the echo time for the associated echo.

2.1.4. Weighted field map computation

Field map estimation is accomplished with a weighted linear regression model. Since signal decay increases with echo time, SNR at later echoes tends to be lower than at earlier echoes, especially in areas of high susceptibility. To reduce the influence of voxels with low signal on the field map estimation, we weight by the squared magnitude of the signal at each echo time. Solving for Eq. (2) then becomes a weighted least squares problem:

$$W\phi\left(\vec{r}\right) = Wf\left(\vec{r}\right)\boldsymbol{t}, \tag{7}$$

where W is a diagonal weight matrix containing the magnitude of the signal at each echo time, $\phi\left(\vec{r}\right)$ is the vector of phase values at each echo time for each voxel, and $\boldsymbol{t}$ is the vector of echo times. Eq. (7) is computed for each frame to yield a field map time series corresponding to each frame of the ME-fMRI time series.

2.1.5. Low rank approximation

To reduce the effects of temporal noise components in the field maps, we employ a low rank approximation approach. This step represents a key technical advancement, as it removes large field changes along the borders of the brain, where spurious changes in the field map are common due to a lack of signal or high measurement noise. The low rank approximation problem can be formulated as follows:

$$\min_{\hat{f}} \left\| f - \hat{f} \right\|_2 \text{ subject to } rank\left(\hat{f}\right) \leq n, \tag{8}$$

where f is the field map time series, reshaped as an $N \times T$ matrix (where N is the voxel dimension and T is the time dimension), $\hat{f}$ is the low rank approximation of f, and n is the rank of the approximation. The solution to Eq. (8) is given by the Eckart–Young–Mirsky theorem (Eckart & Young, 1936), which is simply the n-truncated singular value decomposition of f:

$$\hat{f} = U\Sigma_n V^T, \tag{9}$$

where U and V are the left and right singular vectors of f, respectively, and Σ_n is the diagonal matrix of the first n singular values of f. For the solution estimated from Eq. (9) in our results, we used $n = 10$.

2.1.6. Displacement field inversion

Finally, to obtain the final field map in the undistorted space, each frame of the field map time series is converted to a displacement field using the readout time and voxel size of the data. This displacement field is then inverted to the nearest diffeomorphic inverse to obtain the final field map in the undistorted space. Displacement field inversion was performed using the *InvertDisplacementFieldImageFilter* of the ITK library (McCormick et al., 2014).

2.2. Data acquisition

2.2.1. Head motion and low-motion datasets

Head motion data were collected on an adult participant to assess MEDIC's capability in measuring and correcting

B0 field changes due to head movement. Prior to the motion trials, 3 TOPUP spin-echo field map pairs (TR: 8 s, TE: 66 ms, 72 Slices, FOV: 110 × 110, Voxel Size: 2.0 mm) were collected using a 3T whole-body scanner (Prisma, Siemens Healthcare) with the head in a neutral position. The participants were then asked to rotate their head along each cardinal axis of the scanner, holding each head position for ~3 minutes. Magnitude/phase ME-fMRI data (TR: 1.761 s, TEs: 14.2, 38.93, 63.66, 88.39, 113.12 ms, 72 Slices, FOV: 110 × 110, Voxel Size: 2.0 mm, Multi-Band: 6, iPAT: 2) were collected for the duration of each head position.

To serve as a reference for highly precise resting-state functional connectivity data, an additional low-motion dataset consisting of ~150 minutes of ME-fMRI data was collected over four scanning sessions. For anatomical images, T1w (Multi-echo MPRAGE, TR: 2.5 s, TEs: 1.81, 3.6, 5.39, 7.18 ms, 208 Slices, FOV: 300 × 300, Voxel Size: 0.8 mm, Bandwidth: 745 Hz/px) and T2w (T2 SPACE, TR: 3.2, TE: 565 ms, 176 Slices, Turbo Factor: 190, FOV: 256 × 256, Voxel Size: 1 mm, Bandwidth: 240 Hz/px) were collected. Written informed consent was obtained from the participant for being included in the study.

2.2.2. *Adolescent dataset*

A dataset with 21 participants was acquired to assess MEDIC's distortion correction performance on a group level (ages: 9–12 years; 8 M, 13F; 15 Control, 1 ASD, 6 ADHD). TOPUP spin-echo field maps (TR: 8 s, TE: 66 ms, 72 Slices, FOV: 110 × 110, Voxel Size: 2.0 mm) and magnitude/phase ME-fMRI data (TR: 1.761 s, TEs: 14.2, 38.93, 63.66, 88.39, 113.12 ms, 72 Slices, FOV: 110 × 110, Voxel Size: 2.0 mm, Multi-Band: 6, iPAT: 2) were collected using a 3T whole-body scanner (Prisma, Siemens Healthcare). For each participant, three scans of ME-fMRI data were collected (2× ~16 minutes, 1× ~10 minutes) across 2–5 sessions. For anatomical images, T1w (MPRAGE, TR: 2.5 s, TEs: 2.9 ms, 176 Slices, FOV: 256 × 256, Voxel Size: 1.0 mm, Bandwidth: 240 Hz/px) and T2w (T2 SPACE, TR: 3.2, TE: 565 ms, 176 Slices, Turbo Factor: 200, FOV: 256 × 256, Voxel Size: 1 mm, Bandwidth: 4882 Hz/px) images were also collected. Real time motion monitoring was used during all acquisitions (Dosenbach et al., 2017). Written informed consent was obtained from all participants for being included in the study.

2.2.3. *UMinn dataset*

A single adult participant (age: 25 years) with TOPUP spin-echo field maps (TR: 8 s, TE: 66 ms, 72 Slices, FOV: 110 × 110, Voxel Size: 2.0 mm) and magnitude/phase ME-fMRI data (TR: 1.761 s, TEs: 14.2, 38.93, 63.66, 88.39, 113.12 ms, 72 Slices, FOV: 110 × 110, Voxel Size: 2.0 mm, Multi-Band: 6, iPAT: 2) was collected using a 3T whole-body scanner (Prisma, Siemens Healthcare). ME-fMRI data were collected over four sessions, with a total of ~174 minutes of resting-state data acquired. For anatomical images, T1w (MPRAGE, TR: 2.5 s, TEs: 2.9 ms, 176 Slices, FOV: 256 × 256, Voxel Size: 1.0 mm, Bandwidth: 240 Hz/px) and T2w (T2 SPACE, TR: 3.2, TE: 565 ms, 176 Slices, Turbo Factor: 190, FOV: 256 × 256, Voxel Size: 1 mm, Bandwidth: 240 Hz/px) were collected. Written informed consent was obtained from all participants for being included in the study.

2.2.4. *Penn dataset*

A single adult participant (age: 30 years) with TOPUP spin-echo field maps (TR: 8 s, TE: 66 ms, 72 Slices, FOV: 110 × 110, Voxel Size: 2.0 mm) and magnitude/phase ME-fMRI data (TR: 1.761 s, TEs: 14.2, 38.93, 63.66, 88.39, 113.12 ms, 72 Slices, FOV: 110 × 110, Voxel Size: 2.0 mm, Multi-Band: 6, iPAT: 2) was collected using a 3T whole-body scanner (Prisma, Siemens Healthcare). Two ~6-minute scans of resting-stage ME-fMRI data were collected. For anatomical images, only a T1w (MPRAGE, TR: 2.5 s, TEs: 2.9 ms, 176 Slices, FOV: 256 × 256, Voxel Size: 1.0 mm, Bandwidth: 240 Hz/px) image was collected. Written informed consent was obtained from all participants for being included in the study.

2.2.5. *ABCD dataset*

A large-scale group averaged resting-state functional connectivity map from the Adolescent Brain Cognitive Development (ABCD) study was used to compare individual functional connectivity with averaged group data. This group average map used strict denoising (N = 3,928; > 8 minutes; RSFC data post frame censoring at a filtered frame-wise displacement < 0.08 mm) to remove the effects of nuisance variables such as head motion and respiration (Marek et al., 2022). During ABCD data preprocessing, FSL TOPUP was used for distortion correction. More information on ABCD dataset processing is found in Jernigan et al. (2018).

2.3. Processing pipeline

We compared MEDIC's dynamic distortion correction with the gold standard of static distortion correction, FSL TOPUP (Andersson et al., 2003). For all comparisons, a common pipeline was used where all processing steps were kept the same, with the exception of the distortion correction method. Intensity correction was not performed, as the main focus was distortion correction. For the MEDIC pipeline, field maps were computed and corrected for each frame of the ME-fMRI data using MEDIC. For the TOPUP pipeline, field maps were processed using FSL TOPUP (Andersson et al., 2003), then coregistered to a frame of the ME-fMRI data using 4dfp tools (https://4dfp.readthedocs.io/en/latest/). The same field map was then applied to each frame of the ME-fMRI for distortion correction. Note that for the low-motion dataset, only TOPUP correction was used as a distortion correction method during preprocessing.

Both T1w and T2w anatomical data were processed by debiasing using FSL FAST (Smith et al., 2004) before passing into Freesurfer for anatomical segmentation (Fischl, 2012). Anatomical data were then aligned to the MNI152 atlas (V. Fonov et al., 2011; V. S. Fonov et al., 2009) using 4dfp tools. For ME-fMRI data, slice time correction and motion correction were performed using 4dfp tools. Bias field correction of the ME-fMRI data was performed using N4 Bias field correction (Avants et al., 2009). Coregistration of the functional data to the anatomical data via the T2w image was performed using 4dfp tools. The final atlas-aligned functional data were computed using a one-step resampling of the concatenated transforms (motion correction, distortion correction, functional to anatomical coregistration, anatomical to atlas coregistration) using FSL applywarp (Smith et al., 2004). The ME-fMRI data were combined into an optimally weighted combined image prior to nuisance regression and mapping to the surface using Connectome Workbench (Marcus et al., 2011). Frame censoring was applied to remove the effects of head motion using an FD threshold of 0.08 after filtering for respiration (Fair et al., 2020).

3. RESULTS

3.1. MEDIC captures magnetic field changes due to head motion

Changes in the B0 magnetic field due to head motion are primarily attributable to the shifting position of susceptibility sources relative to the main magnetic field. Unlike traditional static field map methods, MEDIC field maps capture these dynamic alterations in a frame-wise manner. To demonstrate the efficacy of MEDIC in capturing magnetic field changes due to motion, we collected data while participants rotated their head about each of the cardinal axes, in addition to acquiring data in a neutral head position. Dynamic field maps were then extracted from the phase information of the resulting scans using MEDIC. The difference between field maps acquired in the neutral and rotated head positions was subsequently calculated (Neutral–Rotation). Average and standard deviation motion parameters for each head position are documented in Supplementary Table S1.

As the participants rotated their head relative to the neutral resting head position, we observed changes in the B0 field estimated from the frame-wise field maps (Fig. 1 and Supplementary Videos S1–S6). To measure the change in B0 inhomogeneity due to head motion, the field maps for each head rotation were rigid-body realigned to the neutral head position and the difference was computed (Neutral–Rotation). Exemplar frames of the acquired data show the participants rotating their head along each of the cardinal axes in the scanner throughout the time series (Fig. 1a). We found that rotations about the slice direction (Z-axis) led to small changes in the field map (Fig. 1b). In contrast, rotations about the readout (X-axis) and phase-encoding (Y-axis) directions caused significant changes in the field map (Fig. 1b), suggesting that MEDIC-derived field maps are sensitive to changes in the B0 field due to motion. For the particular ME-fMRI sequence used, for every change of 10 Hz in the B0 field, each voxel is displaced by ~0.6 mm. For rotations about the slice direction, the patterns of change observed in the field map were similar to those seen with rotations about the phase-encoding direction, although substantially lower in amplitude. We largely attribute these spatial similarities to the small Y-axis rotations present in the Z-axis rotation data (Supplementary Table S1), likely due to biomechanical constraints in the head and neck.

3.2. MEDIC dynamic distortion correction reduces the impact of head motion on functional connectivity estimates

To assess the effects of these B0 field changes on resting-state functional connectivity (RSFC) analyses, as well as the ability for MEDIC to mitigate them, we compared the functional connectivity maps of data derived from this head motion study with a low motion dataset from the same participant. These data were preprocessed (see Section 2) and distortion corrected separately using both MEDIC and FSL TOPUP, the current gold standard in distortion correction. A separately acquired field map scan in the neutral head position (Frame 50, Fig. 1a) was used for TOPUP distortion correction, reflecting a typical data acquisition experiment of a single field map acquisition at the beginning of a functional scan (See Supplemental Fig. S1). Both MEDIC and TOPUP preprocessed data were projected to the surface. Functional connectivity maps were computed from seeds in the dorso-lateral

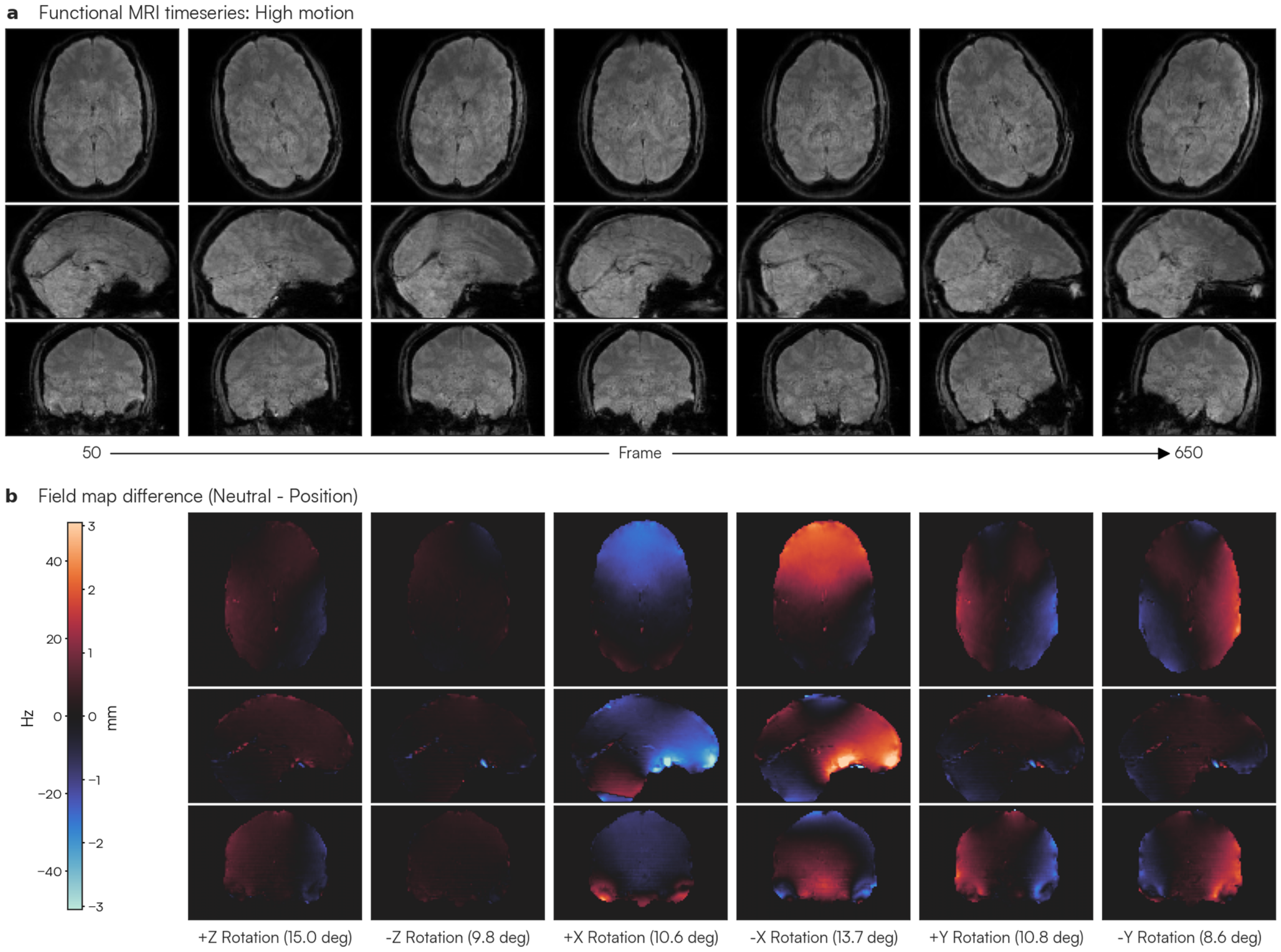

Fig. 1. Changes in main magnetic field (B0) inhomogeneity due to head rotation. To assess the effects of head motion on the B0 magnetic field, the participants rotated their head about each of the three cardinal axes: rotations about the (z) slice axis (i.e., yaw), rotations about the (x) readout axis (i.e., pitch), and rotations about the (y) phase-encoding axis (i.e., roll). Each rotated head position was held for 100 frames (~3 minutes). (a) Selected images from the fMRI time series as the participants rotate their head about each axis (700 frames: ~20 minutes). (b) Field maps for each rotated head position were computed using MEDIC and compared with the MEDIC field map computed in the neutral (i.e., no rotation) head position. The average magnitude of rotation about each major axis is listed for each column and corresponds to each rotated head position in (a). Warmer colors indicate an increase in the B0 inhomogeneity and a voxel shift that is more posterior than the neutral position, while cooler colors indicate the opposite.

prefrontal cortex (DLPFC), the extrastriate visual cortex, and the somato-cognitive action network (SCAN) region of primary motor cortex (Gordon et al., 2023). To assess the effectiveness of distortion correction, the quality of these maps was evaluated by comparing them to a large, low-motion dataset from the same participant, processed with TOPUP.

The exemplar seed maps show that high-motion MEDIC-corrected data had a higher spatial correlation to the low-motion data than TOPUP-corrected high-motion data, despite the low-motion (gold standard) data being processed with TOPUP (Fig. 2). Greater improvement in similarity to the low-motion data was observed in DLPFC (Fig. 2) and occipital cortex (Supplemental Fig. S2a) compared with SCAN (Supplemental Fig. S2b). We observed that the mean correlation between high-motion MEDIC-corrected seed maps and low-motion seed maps was r = 0.35 (SD: 0.16). In contrast, the mean correlation between high-motion TOPUP-corrected seed maps and low-motion data was r = 0.33 (SD: 0.16). Using a two-tailed paired t-test, we found this difference to be statistically significant (two-tailed paired t = 41.4; p < 0.001; df = 59411), indicating that MEDIC-corrected data are more similar to low-motion-corrected data and has greater robustness to head motion. Furthermore, we confirmed that MEDIC and TOPUP yield nearly identical results in the absence of high motion; low-motion MEDIC-corrected data showed an exceptionally high correlation

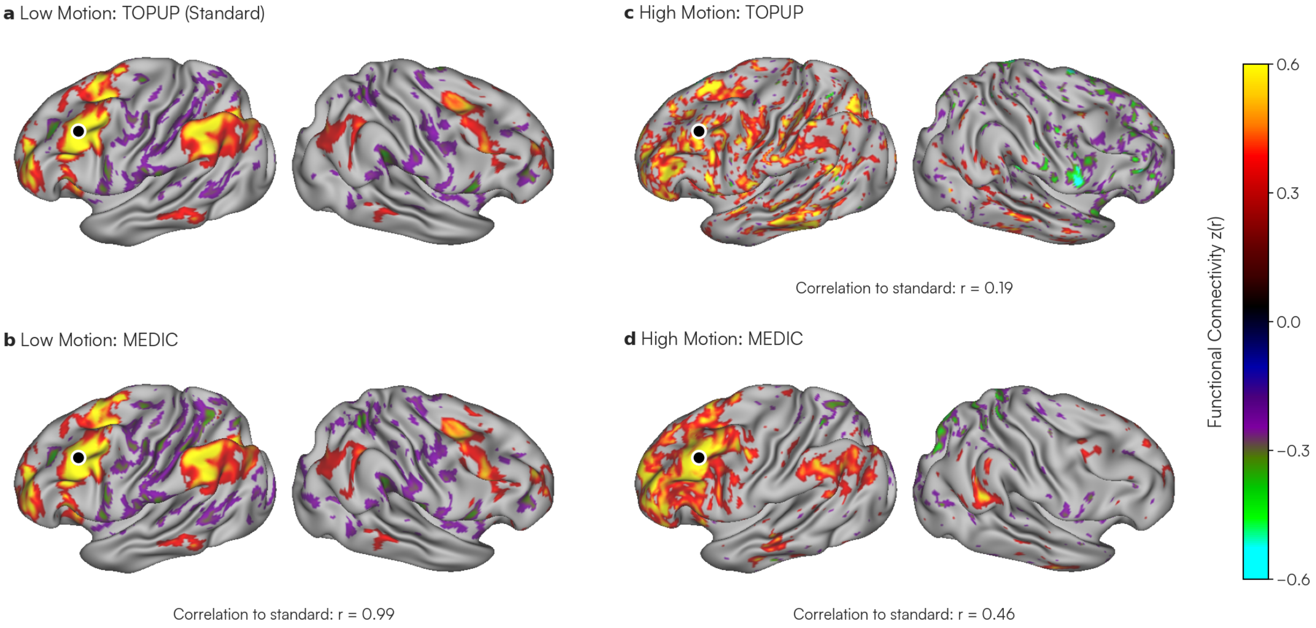

Fig. 2. Comparison of dynamic (MEDIC) and static (TOPUP) distortion correction in low- and high-motion data. To compare the effects of each distortion correction method, resting-state functional connectivity (RSFC) maps were generated for one participant using an exemplar seed in the left dorsolateral prefrontal cortex (DLPFC; marked by a black dot). (a) A low-motion dataset (5100 frames: ~150 minutes) processed using TOPUP; this seed map was used as a reference standard for comparison. (b) The same low-motion dataset processed using MEDIC. (c) A high-motion dataset (700 frames: ~20 minutes) processed using TOPUP (see Supplemental Fig. S1 for the TOPUP field map used). (d) The same high-motion dataset processed using MEDIC. Correlations with the low-motion TOPUP standard are displayed under each seed map. All maps are Fisher z-transformed and thresholded at $|z(r)| > 0.25$ for visualization. Additional exemplar seed maps for occipital and somato-cognitive action network (SCAN) regions are provided in Supplemental Figure S2.

with the TOPUP standard across our exemplar seeds (r = 0.99; Fig. 2 and Supplemental Fig. S2) and across all cortical seeds (mean r = 0.96, SD: 0.07).

3.3. MEDIC dynamic distortion correction improves functional connectivity in pediatric populations

Uncorrected geometric distortion introduces participant-to-participant variability in RSFC structure. We reasoned that improved distortion correction would produce individual RSFC estimates that align more closely with a group average. To accomplish this, we compared MEDIC and TOPUP distortion-corrected FC maps with gold-standard group-averaged data, processed with TOPUP (ABCD Study; N = 3,928) (Marek et al., 2022). We used our Adolescent dataset containing repeated-sampling precision ME-fMRI data from 21 participants (9–12 years old, 8 M, 13F), with a total of 185 runs. These ME-fMRI data were preprocessed with both MEDIC and TOPUP for resting-state functional connectivity analyses.

Seed maps from both MEDIC and TOPUP processed data were compared with the ABCD group-averaged data (Fig. 3a; left). In the occipital cortex, the TOPUP-corrected data showed correlations not observed in the ABCD group (Fig. 3a, right: seed correlation to group-averaged data r = 0.04) that were removed by reprocessing the identical data with MEDIC (Fig. 3a, middle: seed correlation to group-averaged data r = 0.44) (Squared Error: MEDIC = 0.03 (SD: 0.07), TOPUP = 0.07 (SD: 0.10); two-tailed paired t = -84.6; $p < 0.001$; df = 59411).

To quantify the benefits of dynamic distortion correction with MEDIC across the entire Adolescent dataset, cortical seed maps at every vertex for each scan were compared with the corresponding group-averaged standard map (ABCD) through spatial correlations. These spatial correlations were then averaged across all vertices (Fig. 3b; y-axis). The same assessment was done with TOPUP (Fig. 3b; x-axis). MEDIC-corrected data were overall more similar to the ABCD group average compared with TOPUP-corrected data (MEDIC: 147; TOPUP: 38; two-tailed paired t = 9.37; $p < 0.001$; df = 184).

Finally, we sought to understand the regions in which MEDIC improved distortion correction. We examined the spatial pattern of distortion correction differences by doing a vertex-wise paired t-test to generate a vertex-wise t-statistic whole-brain map showing those regions where MEDIC was more similar to the group-averaged data (Fig. 3c; hot colors). A clustering based multiple comparisons correction was applied to correct to a significance level of 0.05 (uncorrected p-value 0.01) and leaving only

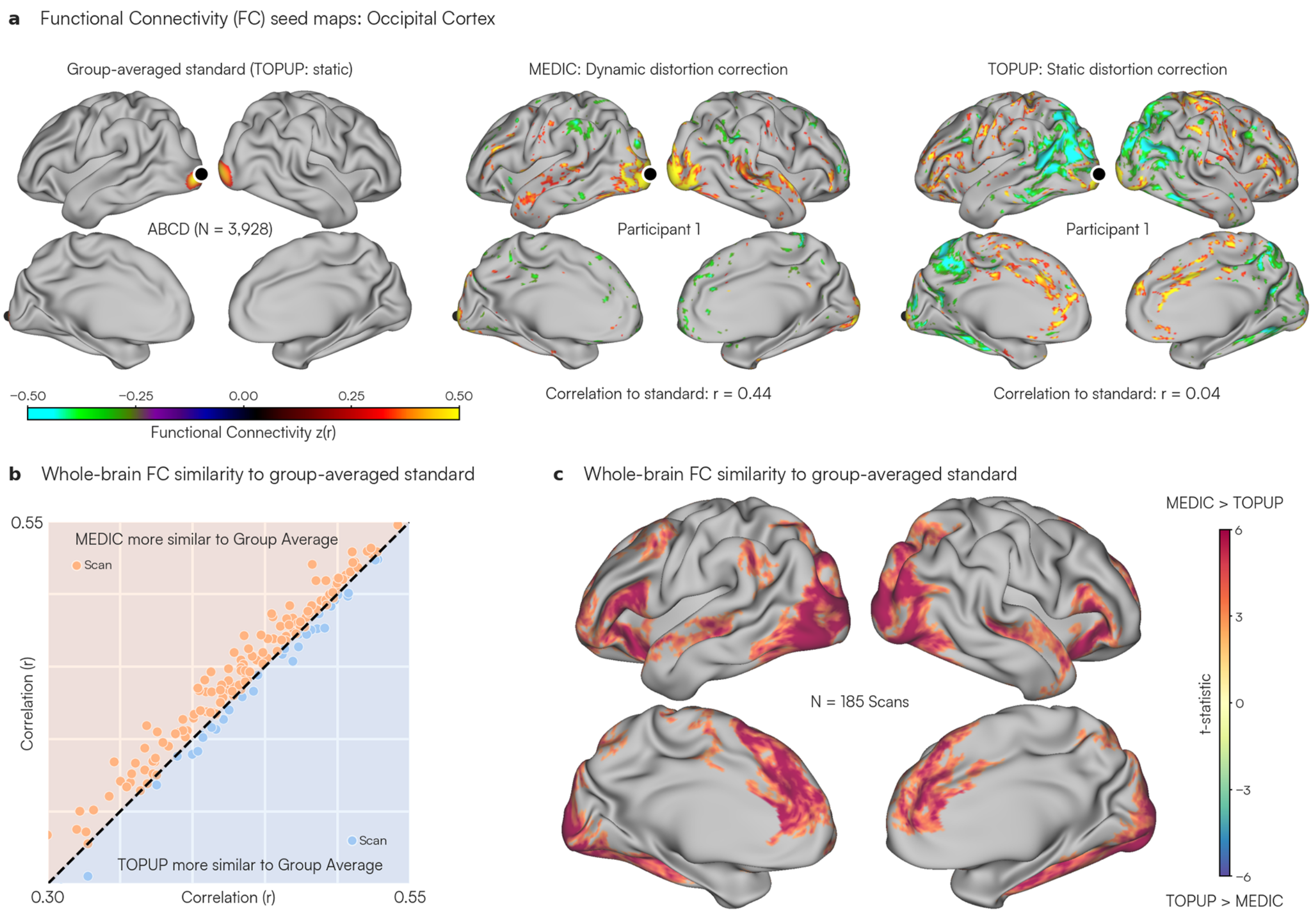

Fig. 3. Comparison of dynamic (MEDIC) and static (TOPUP) distortion correction against large-sample group-averaged data. (a) Resting-state functional connectivity maps from a single scan (~16 minutes) in the Adolescent dataset (N = 185). A seed placed in the occipital cortex (primary visual) is indicated by a black dot. Seed maps are displayed for data corrected using MEDIC (middle) and TOPUP (right) and compared with a functional connectivity map computed from the ABCD group (N = 3,928) average (left). Seed maps are thresholded to only display connectivity values above $|z(r)| > 0.3$ for easier visualization. (b) Mean correlation of each scan from the Adolescent dataset to the ABCD group average. Each dot represents the mean similarity of a single scan (~10–16 minutes) of the Adolescent dataset to the ABCD group average. The y-axis represents the similarity to the ABCD group average using MEDIC correction while the x-axis represents the similarity for the TOPUP-corrected version of the same data. The unity line represents the case where the MEDIC and TOPUP corrections achieved the same similarity to the group-averaged standard. Points that are orange and above the unity line indicate MEDIC-corrected data that were on average more similar to the ABCD group average than TOPUP-corrected data. Blue dots that are below the unity line indicate the opposite. (c) T-statistic map representing the spatial distribution of similarity to the ABCD group average. Each vertex on the surface represents a t-statistic value, estimated using a two-tailed paired t-test across all 185 scans of the Adolescent dataset between MEDIC and TOPUP correction. Warmer (red) colors indicated that MEDIC correction had higher similarity to the ABCD group average compared with TOPUP for that vertex, while cooler (blue) colors indicate the opposite.

statistically significant clusters. This whole-brain map of similarity to the group average revealed that the benefits of using MEDIC dynamic distortion correction were greatest in the medial prefrontal and occipital cortex (Fig. 3c).

3.4. MEDIC frame-wise distortion correction produces superior anatomical alignment

One goal of distortion correction is to improve co-registration of the fMRI to the anatomical data. Therefore, we assessed alignment accuracy by using the gray and white matter surfaces generated from anatomical segmentations (Montez et al., 2023). When distortion correction is optimal, the gray and white matter surfaces obtained from anatomical data should also delineate the gray and white matter voxels in functional data on both the cortical and cerebellar surfaces. For this assessment, data from three separate SIEMENS Prisma MRI scanners at three different institutions: Washington University in St. Louis (WashU, selected participant from the Adolescent dataset), University of Minnesota (UMinn), and University of Pennsylvania (Penn) were processed and distortion corrected using MEDIC and TOPUP. We used participants from three different scanning sites to eliminate scanner-specific effects in the comparison between MEDIC and TOPUP anatomical alignment. Gray and white matter surfaces produced by anatomical segmentations from Freesurfer 7.3.2 (Fischl, 2012) were overlaid on the averaged, atlas-aligned, distortion-corrected functional volumes.

Along the slice-encoding direction, large field map differences between MEDIC and TOPUP were found to occur in select slices in each dataset (Fig. 4; top row). In these regions, we hypothesized that we would also exhibit observable differences in registration to anatomy. This appeared to be the case; and further, in all of these regions, the MEDIC image was better aligned to the anatomy than to the TOPUP image (Fig. 4; middle and bottom row).

In the WashU dataset (Fig. 4a), the most prominent difference was observed in the cerebellum. In the TOPUP-corrected data, the inferior cerebellum was shifted approximately 3 mm anteriorly compared with the anatomical segmentation reference. MEDIC-corrected data closely aligned with the cerebellar anatomy, suggesting a higher efficacy for cerebellar alignment. For the UMinn

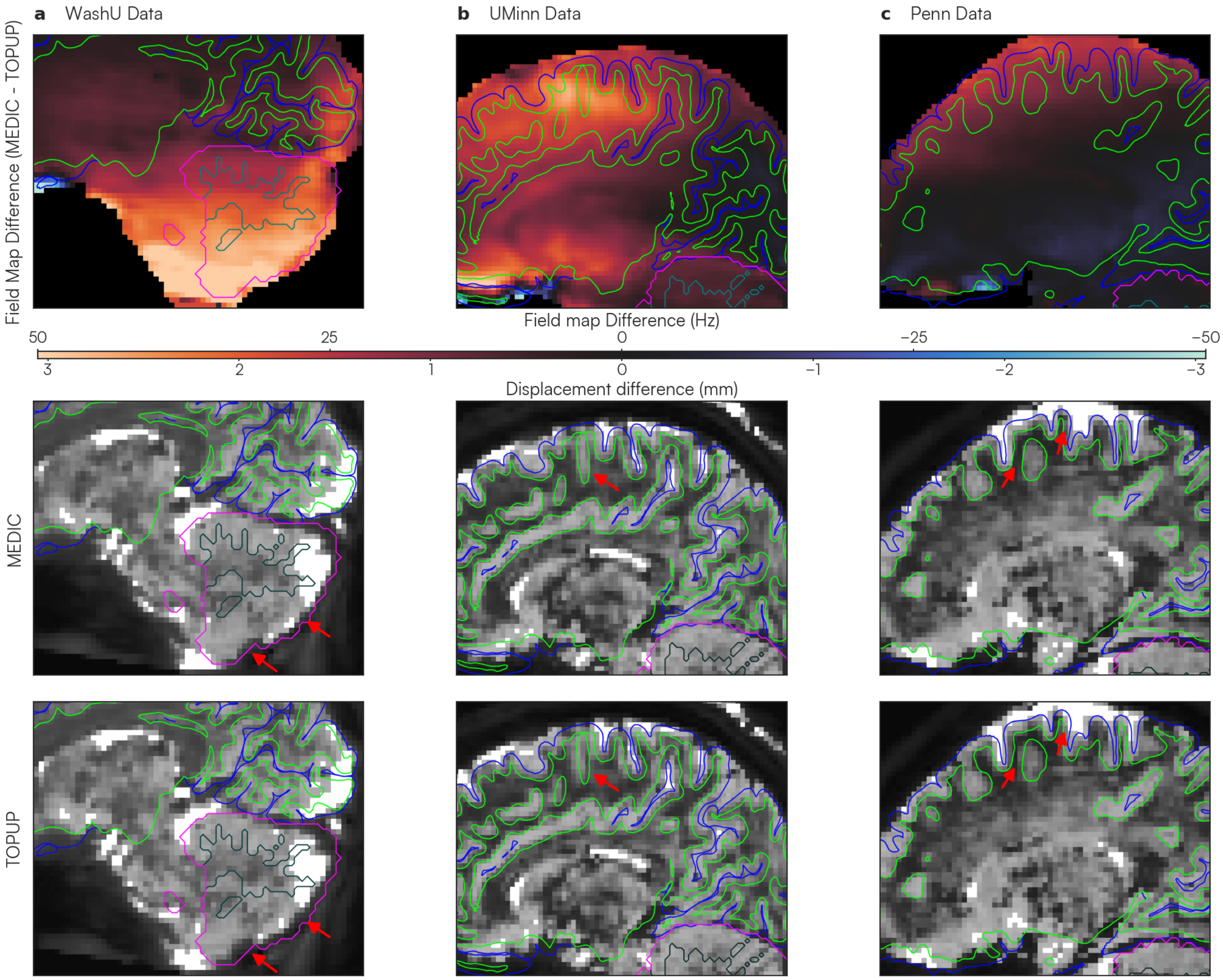

Fig. 4. Comparisons of anatomical surface alignment after dynamic (MEDIC) and static (TOPUP) distortion correction. Gray and white matter boundaries (blue and green outlines, respectively, for cortex; fuchsia and teal outlines, respectively, for cerebellum) were derived from freesurfer anatomical segmentations. Good alignment occurs when segmentation surfaces correctly delineate gray and white matter boundaries of the underlying functional data. Each column shows ME-fMRI data obtained from three different scanning sites: (a) WashU (selected participant from Adolescent dataset), (b) UMinn, and (c) Penn. The top row shows the difference in field maps between MEDIC and TOPUP (MEDIC - TOPUP). The color bar denotes the magnitude of these differences, where warmer colors indicate TOPUP field maps had a lower B0 frequency and have a displacement that is more anterior than MEDIC for a particular voxel. The middle and bottom rows show anatomical surface overlays on the averaged, atlas-aligned ME-fMRI data. Red arrows indicate areas that MEDIC-corrected data were more saliently aligned to the anatomical data than to TOPUP-corrected data.

dataset (Fig. 4b), we identified discrepancies in the dorsal cerebral cortex. The sulci in the TOPUP-corrected images were shifted 2–3 mm anteriorly relative to the anatomical reference. In contrast, the MEDIC-corrected data showed a good agreement with the cortical anatomy. Finally, in the Penn dataset (Fig. 4c), a distortion profile similar to that of the UMinn data was observed. Specifically, the greatest differences appeared in the dorsal cortical region. The TOPUP-corrected data displayed a 1–2 mm anterior shift in cortical structures relative to the anatomical reference. Meanwhile, the MEDIC-corrected data maintained good alignment with the cortical anatomy.

3.5. MEDIC distortion correction is superior on local and global anatomical alignment metrics

To quantify anatomical alignment performance for MEDIC and TOPUP, we computed established local and global alignment metrics (Montez et al., 2023) between distortion-corrected functional data and their corresponding T1w and T2w anatomical data (full statistical tables for each alignment metric are given in Supplementary Table S2). We computed all alignment metrics for the Adolescent dataset across 185 scans from 21 participants in both MEDIC and TOPUP-corrected data.

To assess local image correspondence, we computed the squared correlation (R^2) within a "spotlight", a three-voxel radius sphere window, between each of T1w and T2w anatomical and the reference functional image. Two tailed paired t-tests were computed for each voxel across all functional data scans in the Adolescent dataset (N = 185) to determine which distortion correction strategy was more similar to the anatomy at a local spotlight. Clustering-based multiple comparisons correction was applied to correct to a significance level of 0.05 (uncorrected p-value 0.01). Higher t-statistic values indicated MEDIC was more similar to the anatomical image than TOPUP (Fig. 5). MEDIC distortion-corrected data had higher local similarity to the anatomical data than TOPUP distortion-corrected data in gray matter. Areas where TOPUP performed better were restricted to areas of white matter and CSF, particularly in white matter areas adjacent to the lateral ventricle.

Further quantifying the local similarity, we computed the mean of R^2 values across all spotlights for each scan (Fig. 6a). MEDIC significantly outperformed static TOPUP correction in both the T1w R^2 spotlight (MEDIC = 0.068 (SD: 0.007); TOPUP = 0.066 (SD: 0.008); two-tailed paired t = 7.133; p < 0.001; df = 184) and T2w R^2 spotlight (MEDIC = 0.083 (SD: 0.010); TOPUP = 0.081 (SD: 0.011); two-tailed paired t = 6.124; p < 0.001; df = 184) analyses.

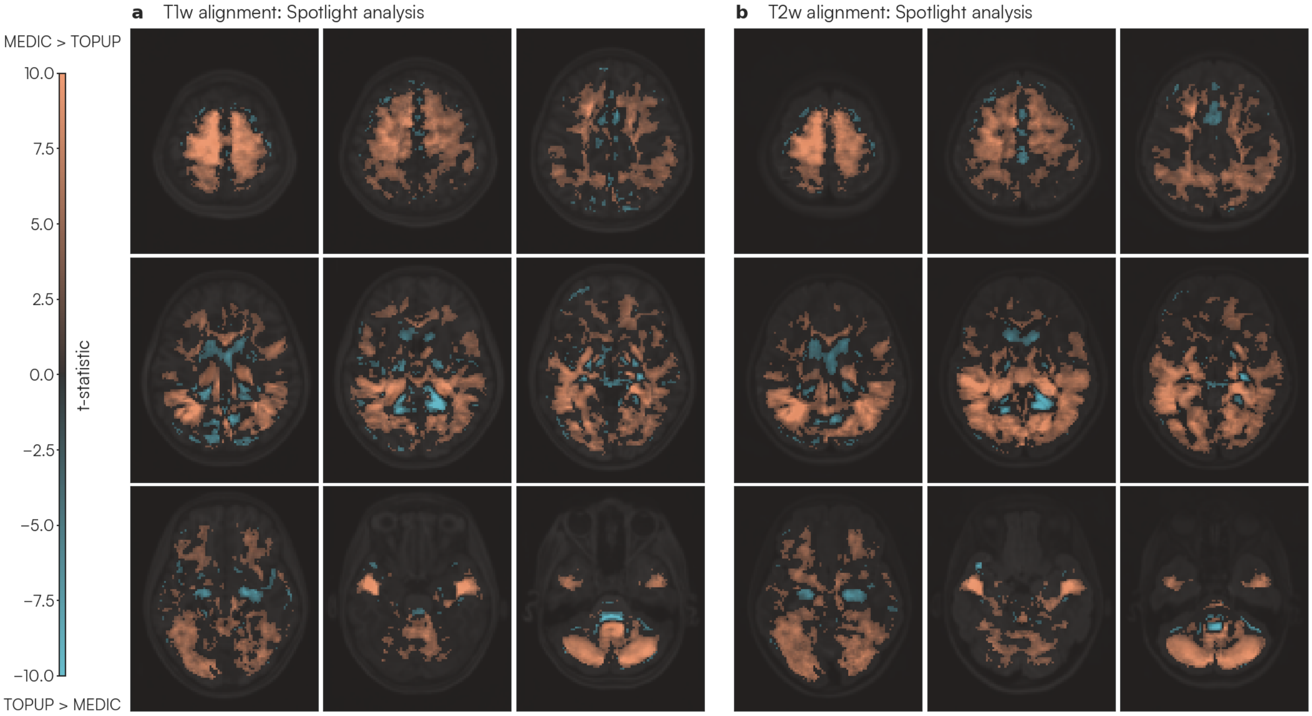

Fig. 5. Spotlight assessment of local similarity between distortion-corrected functional and T1w/T2w anatomical data. T-statistic maps from local R^2 values were computed using a three-voxel radius "spotlight" moving across the entire image. (a) shows the t-statistic between MEDIC and TOPUP for each R^2 spotlight between the functional image and the T1w anatomical image, while (b) shows the t-statistic between MEDIC and TOPUP for each R^2 spotlight between the functional image and the T2w anatomical image. Warmer colors indicate MEDIC-corrected data had higher local similarity to anatomy than TOPUP-corrected data.

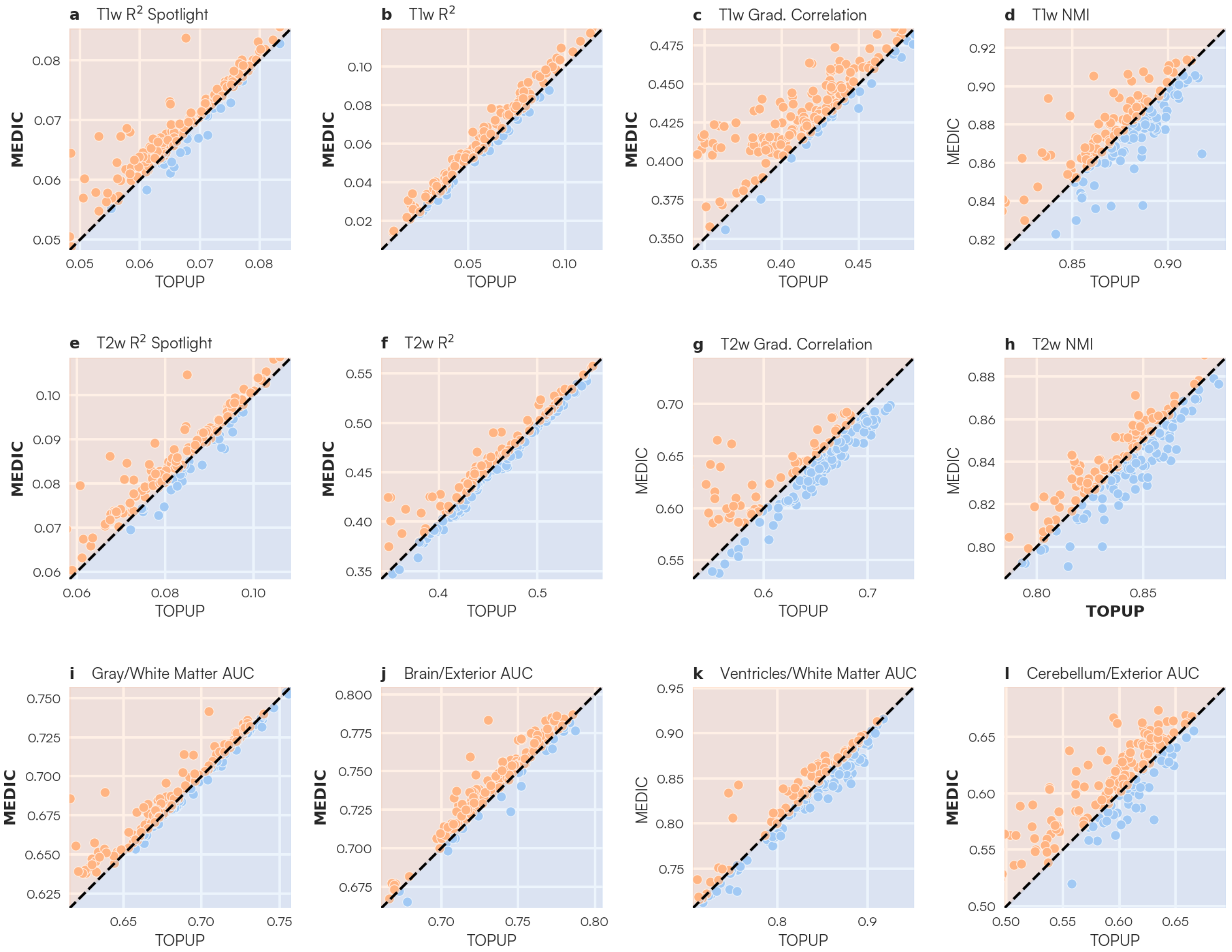

Fig. 6. Anatomical alignment metrics comparing MEDIC and TOPUP distortion correction methods. Distortion-corrected functional images from each distortion correction method were compared against each T1w/T2w anatomical image for each alignment measure, where bar plots for each metric are displayed. Each bar plot represents the distribution of each anatomical alignment metric on each scan of the Adolescent dataset (N = 185). Orange bars indicate data corrected with MEDIC, while blue bars indicate data corrected with TOPUP. Bolded labels indicate that the alignment metric was statistically significant in favor of the method. (a, e) Spatial mean R^2 of local spotlight metric for both T1w and T2w images (see also Fig. 5). Higher values indicate that a scan had, on average, higher local similarity to the anatomical images. Global alignment metrics such as (b, f) R^2, (c, g) correlation of the gradient magnitude, and (d, h) normalized mutual information assess global correspondence of the distortion-corrected functional data to T1w and T2w anatomical images (Montez et al., 2023). Higher values indicate greater global image similarity to the anatomical image. (i, j, k, l) Segmentation metrics assessing accuracy of freesurfer based tissue segmentation on each functional image. Higher AUC values indicate that the anatomical segmentation was able to better discriminate between tissue types.

To assess global image correspondence, we used multiple global metrics such as the squared correlation (R^2), correlation of the gradient magnitude, and normalized mutual information (NMI) between each distortion-corrected functional image and each T1w and T2w anatomical image (Fig. 6b) (Montez et al., 2023). MEDIC significantly outperformed TOPUP on both T1w R^2 (MEDIC = 0.063 (SD: 0.028); TOPUP = 0.060 (SD: 0.028); two-tailed paired t = 11.284; p < 0.001; df = 184) and T2w R^2 (MEDIC = 0.457 (SD: 0.053); TOPUP = 0.454 (SD: 0.056); two-tailed paired t = 2.729; p = 0.007; df = 184) metrics, as well as the T1w gradient correlation (MEDIC = 0.43 (SD: 0.028); TOPUP = 0.414 (SD: 0.036); two-tailed paired t = 11.727; p < 0.001; df = 184) metric. TOPUP slightly outperformed MEDIC on the T2w NMI (MEDIC = 0.836 (SD: 0.026); TOPUP = 0.838 (SD: 0.026); two-tailed paired t = -1.985; p = 0.049; df = 184) metric.

Finally, we examined alignment along specific tissue boundaries, delineated by the participant's anatomical segmentation (Montez et al., 2023). By overlaying the participant's anatomical segmentation on the time-average fMRI data, and computing the Receiver Operating

Characteristic (ROC) curve, we determined how well each distortion correction method correctly delineated tissue types along specific boundaries by computing the area under the curve (AUC) value (Fig. 6c). MEDIC significantly outperformed TOPUP correction in both the brain/exterior (MEDIC = 0.735 (SD: 0.035); TOPUP = 0.729 (SD: 0.034); two-tailed paired t=11.488; $p < 0.001$; df = 184) the gray/white matter (MEDIC = 0.735 (SD: 0.035); TOPUP = 0.729 (SD: 0.034); two-tailed paired t=11.488; $p < 0.001$; df = 184), and cerebellum/exterior (MEDIC = 0.607 (SD: 0.041); TOPUP = 0.596 (SD: 0.049); two-tailed paired t=5.073; $p < 0.001$; df = 184) boundaries.

4. DISCUSSION

In fMRI studies, distortion of the source images is transmitted downstream, distorting all derived research findings and clinical maps (Haskell et al., 2023). Previously state-of-the-art methods employed static distortion correction techniques that depend on the acquisition of a separate field map image (Andersson et al., 2003; Jezzard & Balaban, 1995). However, static field mapping is limiting and becomes less accurate with larger head displacements during a scan (Andersson et al., 2018; Graham et al., 2017). Given the massive challenge of head motion, especially in children, the elderly, and patient populations (Goto et al., 2016; Greene et al., 2018; Hausman et al., 2022; Makowski et al., 2019), motion robust distortion correction is crucial for the success of fMRI studies in these subpopulations.

Despite the conceptual superiority of dynamic field mapping approaches, prior attempts have not been widely adopted by the neuroimaging community (Visser et al., 2012; Weiskopf et al., 2005). This is largely due to the unavailability of open-source releases of said approaches. With the recent growing interest and use of ME-fMRI for neuroimaging studies, our proposed method, MEDIC, provides researchers the capability to address dynamic B0 changes due to head motion. MEDIC is provided as a freely available open-source tool, and will further motivate the use of ME-fMRI in neuroimaging studies.

4.1. ME-fMRI enhances sensitivity, reliability, and signal coverage in neuroimaging

ME-fMRI has many benefits over single-echo fMRI (SE-fMRI) and has been established for at least a decade (Gowland & Bowtell, 2007; Kundu et al., 2013, 2017). ME-fMRI allows for multiple echoes to be analyzed separately or as an optimally combined time series, which exhibits higher SNR and improves statistical power of analyses in regions of high susceptibility. Multiple echoes also allow for additional denoising capabilities through ME-ICA (Dipasquale et al., 2017; Kundu et al., 2013) or denoising pipelines, such as tedana (DuPre et al., 2021).

Recent neuroimaging breakthroughs, such as the discovery of the somato-cognitive action network (SCAN) in the central sulcus, which was previously thought to be the exclusive domain of effector-specific primary motor cortex (Gordon et al., 2023), utilized ME-fMRI data. ME-fMRI was also used to discover that the ventromedial prefrontal cortex (vmPFC), a region plagued by massive distortions, includes an enlarged salience network node in depression patients (Lynch et al., 2024). Similarly, ME-fMRI was able to identify individual-specific persistent brain changes after a single dose of the psychedelic psilocybin (Siegel et al., 2024), and the stimulant methylphenidate (Kay et al., 2025).

Patient- (clinical) and individual-specific (research) precision functional mapping (PFM) (Gordon et al., 2017) are specific applications of RSFC and task fMRI where ME-fMRI and by extension MEDIC are most valuable. Averaging fMRI data across individuals blurs spatial boundaries, effectively smoothing the underlying data (Fair et al., 2021; Gordon et al., 2023, 2017; Hermosillo et al., 2024; Laumann et al., 2023; Newbold & Dosenbach, 2021; Newbold et al., 2020; Saggar et al., 2022; Zheng et al., 2021). Therefore, group averaging partially obscures the greater spatial precision obtainable with ME-fMRI and MEDIC. Hence, it may not be a coincidence that several strong proponents of ME-fMRI have been using it for PFM, through which greater confidence in spatial details can be directly converted into neuroscientific insights (Gordon et al., 2023; Lynch et al., 2020, 2022, 2024; Siegel et al., 2024). If the goal is individual-specific PFM, then ME-fMRI and MEDIC improve SNR and distortion correction, with the minor cost of slightly longer data processing times and increase in TR. Furthermore, with MEDIC, field map scans can be eliminated from the scanning protocol, eliminating the risk that some field maps end up motion corrupted or lost altogether.

The use of ME-fMRI over SE-fMRI may come at the cost of slightly longer data processing times and an increase in TR, both of which are minor costs at the spatial resolutions typical of most fMRI studies (see Discussion below). ME-fMRI may, however, present challenges when acquiring scans at higher resolutions, as the longer echo-train lengths required limit the number of TEs acquired before signal dropout, or when acquiring scans at higher field strengths, which involves more rapid signal decay. These are important drawbacks to consider, though further advances in acceleration methods and other processing techniques will likely broaden the scope of ME-fMRI, and thus MEDIC as well.

4.2. MEDIC further boosts the capabilities of ME-fMRI through dynamic field map correction

Head motion also impacts distortions by changing the spatial distribution of the B0 field inhomogeneity (Andersson et al., 2018; Graham et al., 2017). Changes to the B0 magnetic field result when someone rotates their head out of the slice plane (i.e., readout and phase-encoding directions). Traditional static field maps cannot account for these time-varying changes to the field, since they only measure the B0 field at a single time point before or after a scan. In addition, any head motion that occurs between the field map acquisition and the fMRI scan will also reduce the accuracy of distortion correction due to localization errors.

Computing the phase evolution across multiple echo times across an ME-fMRI sequence allows one to compute a field map for each data frame, allowing for the tracking of magnetic field (B0) inhomogeneities dynamically and as close to real time as possible. With MEDIC, this results in two main benefits. First, this allows MEDIC to measure the B0 field at each TR, allowing for the measurement of any time-varying changes to the field, such as global oscillations induced by respiration (see Supplemental Fig. S3). Second, since MEDIC field maps are inherently co-registered to the ME-fMRI data they are correcting, they eliminate any errors in co-registration that may arise from separate field map acquisitions.

As a general observation, for every one degree of head rotation outside of the slice plane, we estimated a maximum change in the B0 field of 5 Hz/0.3 mm in our data, representing the maximum error in distortion correction one would obtain by using a static field map. Therefore, any functional connectivity analysis done in the presence of notable head motion would benefit from MEDIC dynamic distortion corrections. In living participants, motion can never be fully eliminated, even when using external devices such as head restraints to mitigate head motion (Power et al., 2019) or sedation, which often is prohibitive in studies. Infants, children, the elderly, and patient populations typically have the highest head motion (Goto et al., 2016; Greene et al., 2018; Hausman et al., 2022; Makowski et al., 2019) and utilization of ME-fMRI and MEDIC will likely be most beneficial in these groups.

4.3. MEDIC provides superior distortion correction due to self-reference

MEDIC field maps generated correction results more similar to group-averaged data than those produced by the TOPUP method. Importantly, this occurred even though the group-averaged data had been distortion corrected using TOPUP—a circumstance that one would assume would inherently be biased toward TOPUP's performance. Notably, we observed greater correspondence between MEDIC and the group-averaged functional connectivity maps within the medial prefrontal cortex and the occipital regions. In addition, there were still large local distortions even after correction with TOPUP, particularly in the dorsal cortical surface and cerebellum.

We attribute MEDIC's superior distortion correction capabilities to the fact that MEDIC uses field maps sourced from the same data it is correcting. This "self-reference" property provides two main benefits: first, fluctuations in head motion may have led to differences in the measured field, which static field maps only measure at a single point in time, potentially causing inaccurate localization of B0 field inhomogeneities and, consequently, less than ideal distortion correction. Second, a single time point static field map might not accurately estimate the B0 field inhomogeneity of the scan it is meant to correct, leading to suboptimal distortion correction. This can result from a mismatch in acquisition parameters from the fMRI and the field map data, leading to differences in affected B0 inhomogeneity. In such cases, MEDIC-based distortion correction is able to correct for additional off-resonance effects.

4.4. On parameter selection in ME-fMRI and MEDIC

Despite the benefits of ME-fMRI, one drawback is the requisite increase in TR due to the collection of additional echoes (Gowland & Bowtell, 2007). For single-echo fMRI acquisitions, echo times are typically ~30 ms (TE). In multi-echo, any additional echo after this time represents the increase in TR over a single-echo acquisition. For example, a three-echo acquisition with echo times of 15 ms, 30 ms, and 45 ms would require an extra 15 ms per RF pulse compared with a single-echo acquisition. This increase in TR can be mitigated if one were to reduce the number of slices, at the cost of a smaller field of view (FOV), or by increasing the parallel imaging acceleration factors, while maintaining the same FOV. Acceleration techniques, including both in-plane undersampling and multi-band (simultaneous multi-slice), are a must if one desires multiple echoes, a TR of ~1 s and resolutions of 2.4 mm or smaller. Most recent ME-fMRI sequences seem to utilize three to five echoes with the second echo around ~30 ms (Aruldass et al., 2021; Cohan et al., 2023; De Cates et al., 2023; Hollarek et al., 2023; Lynch et al., 2020). The acquisition of higher spatial resolution images is additionally challenging with ME-fMRI as even more acceleration is required in order to acquire multiple echoes without unacceptably long readout times and/or TRs.

The addition of MEDIC does not largely change these considerations. In our study, relatively late echo times were used (TE1 = 14.2 ms, TE2 = 38.93 ms) but were still found to be effective at measuring phase and correcting distortion. This robustness is achieved because MEDIC weighs samples by their signal magnitude, allowing it to adapt to regions where signal intensity may drop in certain echoes. In regions where later echoes have significant signal dropout, the correction is primarily driven by earlier echoes that have sufficient signal. The use of earlier echo times may improve the performance of MEDIC even further, particularly in areas of high susceptibility (Port & Pomper, 2000). MEDIC only requires the use of two echoes to compute a field map, which is under the typical acquisition of three to five echoes. However, in cases where users may want to use larger echo spacings, the identifiability of the field map computation may break down, preventing accurate field map estimations. In such cases, more echoes may be preferred to obtain a unique solution.

4.5. MEDIC is computationally efficient and open source

Our open-source implementation of MEDIC is optimized, resulting in computational times comparable with TOPUP for an entire dataset. Overall, the computational time to estimate MEDIC field maps over an entire dataset is generally comparable with the processing time required by TOPUP in its field map estimation process. Computation can be further reduced by running MEDIC's parallel algorithm on a computer with multiple cores.

While previous methods of multi-echo dynamic distortion correction have been suggested (Visser et al., 2012; Weiskopf et al., 2005), lack of functioning open-source implementations of such methods has impeded their adoption. We, therefore, release our implementation of MEDIC as an open-source package, which is found at https://github.com/vanandrew/warpkit. This package is a Python library that can be integrated in a variety of processing pipelines and existing neuroimaging tools with output formats into AFNI, FSL, and ANTs (Avants et al., 2009; Cox, 1996; Smith et al., 2004). For example, while steps such as intensity correction were omitted from both MEDIC and TOPUP in the current study to isolate the effects of distortion correction, MEDIC is fully compatible with existing tools that implement these steps. We hope that this will facilitate the adoption of MEDIC in the neuroimaging community.

4.6. Multi-echo frame-wise distortion correction for motion robust fMRI

MEDIC's dynamic, frame-wise distortion correction is not only conceptually superior to static field-map approaches, but also significantly improves the accuracy of fMRI maps, especially in the presence of head motion. This performance is facilitated by several algorithmic advancements, including temporal phase correction and SVD-based low-rank approximation to ensure stable, denoised field map time series. MEDIC is also easy to implement and use and, despite computing a dynamic field map at each data frame, is no slower than previously standard static distortion correction (i.e., TOPUP). ME-fMRI is recently gaining popularity more rapidly, at least in part due to its benefits for patient- or individual-specific precision functional mapping (PFM) (D'Andrea et al., 2025; Gordon et al., 2017; Krimmel et al., 2025; Lynch et al., 2024). MEDIC's dynamic distortion correction capability provides another driving reason to acquire multi-echo data. For fMRI applications aiming to maximize spatial precision, such as PFM, or intervention and neuromodulation targeting with fMRI, MEDIC provides yet another powerful reason to switch from single- to multi-echo.

DATA AND CODE AVAILABILITY

The implementation for MEDIC is found at https://github.com/vanandrew/warpkit. Code for the processing pipeline is found at https://github.com/DosenbachGreene/processing_pipeline. Code for data analysis and figure generation is found at https://github.com/vanandrew/medic_analysis. Data used in our study are found at https://dosenbachlab.wustl.edu/data.

AUTHOR CONTRIBUTIONS

Conception: A.N.V. and M.D.T. Design: A.N.V., M.D.T., D.F.M., T.O.L, E.M.G., and N.U.F.D. Data acquisition, analysis, and interpretation: A.N.V., D.F.M., T.O.L., P.N.C., V.S., T.M., N.J.B., N.R.-P., K.M.S., J.S.M., F.I.W., B.A., A.R., J.L.R., T.S., K.B.W., A.S., E.M.G., and M.D.T. Manuscript writing and revision: A.N.V., D.F.M., T.O.L., P.N.C., V.S., T.M., N.J.B., N.R.-P., K.M.S., J.S.M., F.I.W., B.A., R.J.C., S.R.K, A.M., A.R., J.L.R., T.S., A.W., K.B.W., A.S., J.S.S, B.P.K, S.M.N., B.T.-C., S.A.M., L.V., E.Y., T.D.S., E.M.G., D.A.F., M.D.T., and N.U.F.D. WashU subject was author N.U.F.D.

DECLARATION OF COMPETING INTEREST

A.N.V., D.A.F., and N.U.F.D. have a financial interest in Turing Medical Inc. and may benefit financially if the company is successful in marketing FIRMM motion monitoring software products. A.N.V., D.A.F., and N.U.F.D. may receive royalty income based on FIRMM technology developed at Washington University School of Medicine and Oregon Health and Sciences University and licensed to Turing Medical Inc. D.A.F. and N.U.F.D. are co-founders of Turing Medical Inc. These potential conflicts of interest have been reviewed and are managed by Washington University School of Medicine, Oregon Health and Sciences University, and the University of Minnesota. A.N.V. is now an employee of Turing Medical Inc. The other authors declare no competing interests.

ACKNOWLEDGMENTS

This work was supported by NIH grants NS123345 (B.P.K.), NS098482 (B.P.K.), MH121518 (S.M.), MH129616 (T.O.L.), T32DA007261 (S.R.K), DA041148 (D.A.F.), DA04112 (D.A.F.), MH115357 (D.A.F.), MH096773 (D.A.F. and N.U.F.D.), MH122066 (E.M.G., D.A.F., and N.U.F.D.), MH121276 (E.M.G., D.A.F., and N.U.F.D.), MH124567 (E.M.G., D.A.F., and N.U.F.D.), NS129521 (E.M.G., D.A.F., and N.U.F.D.), and NS088590 (N.U.F.D.); by the National Spasmodic Dysphonia Association (E.M.G.); by the Taylor Family Foundation (T.O.L.); by the Intellectual and Developmental Disabilities Research Center (N.U.F.D.); by the Kiwanis Foundation (N.U.F.D.); by the Washington University Hope Center for Neurological Disorders (E.M.G., B.P.K., and N.U.F.D.); and by Mallinckrodt Institute of Radiology pilot funding (E.M.G. and N.U.F.D.). Computations were performed using the facilities of the Washington University Research Computing and Informatics Facility, which were partially funded by NIH grants S10OD025200, 1S10RR022984-01A1, and 1S10OD018091-01. Additional support is provided by the McDonnell Center for Systems Neuroscience.

SUPPLEMENTARY MATERIALS

Supplementary material for this article is available with the online version here: https://doi.org/10.1162/IMAG.a.1262#supplementary-data.

REFERENCES

Andersson, J. L. R., Graham, M. S., Drobnjak, I., Zhang, H., & Campbell, J. (2018). Susceptibility-induced distortion that varies due to motion: Correction in diffusion MR without acquiring additional data. *NeuroImage*, *171*, 277–295. https://doi.org/10.1016/j.neuroimage.2017.12.040

Andersson, J. L. R., Skare, S., & Ashburner, J. (2003). How to correct susceptibility distortions in spin-echo echo-planar images: Application to diffusion tensor imaging. *NeuroImage*, *20*(2), 870–888. https://doi.org/10.1016/S1053-8119(03)00336-7

Aruldass, A. R., Kitzbichler, M. G., Morgan, S. E., Lim, S., Lynall, M.-E., Turner, L.; Wellcome Trust Consortium for Neuroimmunology of Mood Disorders and Alzheimer's Disease (NIMA), Cavanagh, J., Cowen, P., Pariante, C. M., Harrison, N. A., & Bullmore, E. T. (2021). Dysconnectivity of a brain functional network was associated with blood inflammatory markers in depression. *Brain, Behavior, and Immunity*, *98*, 299–309. https://doi.org/10.1016/j.bbi.2021.08.226

Avants, B. B., Tustison, N., & Song, G. (2009). Advanced normalization tools (ANTS). *The Insight Journal*, *2*(365), 1–35. https://doi.org/10.54294/uvnhin

Brown, R., Cheng, Y., Haacke, E., Thompson, M., & Venkatesan, R. (2014). *Magnetic resonance imaging: Physical principles and sequence design*. John Wiley & Sons, Incorporated. https://doi.org/10.1002/9781118633953

Cohan, R., Rafique, S. A., Stoby, K. S., Gorbet, D. J., & Steeves, J. K. E. (2023). Continuous and intermittent theta burst stimulation of primary visual cortex do not modulate resting state functional connectivity: A sham-controlled multi-echo fMRI study. *Brain and Behavior*, *13*(5), e2989. https://doi.org/10.1002/brb3.2989

Cox, R. W. (1996). AFNI: Software for analysis and visualization of functional magnetic resonance neuroimages. *Computers and Biomedical Research, an International Journal*, *29*(3), 162–173. https://doi.org/10.1006/cbmr.1996.0014

Cusack, R., Brett, M., & Osswald, K. (2003). An evaluation of the use of magnetic field maps to undistort echo-planar images. *Neuroimage*, *18*(1), 127–142. https://doi.org/10.1006/nimg.2002.1281

De Cates, A. N., Martens, M. A., Wright, L. C., Gibson, D., Spitz, G., Gould Van Praag, C. D., Suri, S., Cowen, P. J., Murphy, S. E., & Harmer, C. J. (2023). 5-HT4 receptor agonist effects on functional connectivity in the human brain: Implications for procognitive action. *Biological Psychiatry: Cognitive Neuroscience and Neuroimaging*, *8*(11), 1124–1134. https://doi.org/10.1016/j.bpsc.2023.03.014

Dipasquale, O., Sethi, A., Laganà, M. M., Baglio, F., Baselli, G., Kundu, P., Harrison, N. A., & Cercignani, M. (2017). Comparing resting state fMRI de-noising approaches using multi- and single-echo acquisitions. *PLoS One*, *12*(3), e0173289. https://doi.org/10.1371/journal.pone.0173289

Dosenbach, N. U. F., Koller, J. M., Earl, E. A., Miranda-Dominguez, O., Klein, R. L., Van, A. N., Snyder, A. Z., Nagel, B. J., Nigg, J. T., Nguyen, A. L., Wesevich, V., Greene, D. J., & Fair, D. A. (2017). Real-time motion analytics during brain MRI improve data quality and reduce costs. *NeuroImage*, *161*, 80–93. https://doi.org/10.1016/j.neuroimage.2017.08.025

DuPre, E., Salo, T., Ahmed, Z., Bandettini, P. A., Bottenhorn, K. L., Caballero-Gaudes, C., Dowdle, L. T., Gonzalez-Castillo, J., Heunis, S., Kundu, P., Laird, A. R., Markello, R., Markiewicz, C. J., Moia, S., Staden, I., Teves, J. B., Uruñuela, E., Vaziri-Pashkam, M., Whitaker, K., & Handwerker, D. A. (2021). TE-dependent analysis of multi-echo fMRI with *tedana*. *Journal of Open Source Software*, *6*(66), 3669. https://doi.org/10.21105/joss.03669

Dymerska, B., Eckstein, K., Bachrata, B., Siow, B., Trattnig, S., Shmueli, K., & Robinson, S. D. (2021). Phase unwrapping with a rapid opensource minimum spanning tree algorithm (ROMEO). *Magnetic Resonance in Medicine*, *85*(4), 2294–2308. https://doi.org/10.1002/mrm.28563

D'Andrea, C. B., Laumann, T. O., Newbold, D. J., Lynch, C. J., Hadji, M., Nelson, S. M., Nielsen, A. N., Chauvin, R. J., Krimmel, S. R., Snyder, A. Z., Marek, S., Greene, D. J., Raichle, M. E., Dosenbach, N. U. F., & Gordon, E. M. (2025). Action-mode subnetworks for decision-making, action control, and feedback. *Proceedings of the National Academy of Sciences*, *122*(27), e2502021122. https://doi.org/10.1073/pnas.2502021122

Eckart, C., & Young, G. (1936). The approximation of one matrix by another of lower rank. *Psychometrika*, *1*(3), 211–218. https://doi.org/10.1007/BF02288367

Eckstein, K., Dymerska, B., Bachrata, B., Bogner, W., Poljanc, K., Trattnig, S., & Robinson, S. D. (2018). Computationally efficient combination of multi-channel phase data from multi-echo acquisitions (ASPIRE). *Magnetic Resonance in Medicine*, *79*(6), 2996–3006. https://doi.org/10.1002/mrm.26963

Fair, D. A., Dosenbach, N. U., Moore, A. H., Satterthwaite, T. D., & Milham, M. P. (2021). Developmental cognitive neuroscience in the era of networks and big data: Strengths, weaknesses, opportunities, and threats. *Annual Review of Developmental Psychology*, *3*(1), 249–275. https://doi.org/10.1146/annurev-devpsych-121318-085124

Fair, D. A., Miranda-Dominguez, O., Snyder, A. Z., Perrone, A., Earl, E. A., Van, A. N., Koller, J. M., Feczko, E., Tisdall, M. D., van der Kouwe, A., Klein, R. L., Mirro, A. E., Hampton, J. M., Adeyemo, B., Laumann, T. O., Gratton, C., Greene, D. J., Schlaggar, B. L., Hagler, D. J., Jr., … Dosenbach, N. U. F. (2020). Correction of respiratory artifacts in MRI head motion estimates. *NeuroImage*, *208*, 116400. https://doi.org/10.1016/j.neuroimage.2019.116400

Fischl, B. (2012). FreeSurfer. *NeuroImage*, *62*(2), 774–781. https://doi.org/10.1016/j.neuroimage.2012.01.021

Fonov, V., Evans, A. C., Botteron, K., Almli, C. R., McKinstry, R. C., & Collins, D. L. (2011). Unbiased average age-appropriate atlases for pediatric studies. *NeuroImage*, *54*(1), 313–327. https://doi.org/10.1016/j.neuroimage.2010.07.033

Fonov, V. S., Evans, A. C., McKinstry, R. C., Almli, C. R., & Collins, D. L. (2009). Unbiased nonlinear average age-appropriate brain templates from birth to adulthood. *NeuroImage*, *47*, S102. https://doi.org/10.1016/S1053-8119(09)70884-5

Gordon, E. M., Chauvin, R. J., Van, A. N., Rajesh, A., Nielsen, A., Newbold, D. J., Lynch, C. J., Seider, N. A., Krimmel, S. R., Scheidter, K. M., Monk, J., Miller, R. L., Metoki, A., Montez, D. F., Zheng, A., Elbau, I., Madison, T., Nishino, T., Myers, M. J., … Dosenbach, N. U. F. (2023). A somato-cognitive action network alternates with effector regions in motor cortex. *Nature*, *617*(7960), 351–359. https://doi.org/10.1038/s41586-023-05964-2

Gordon, E. M., Laumann, T. O., Gilmore, A. W., Newbold, D. J., Greene, D. J., Berg, J. J., Ortega, M., Hoyt-Drazen, C., Gratton, C., Sun, H., Hampton, J. M., Coalson, R. S., Nguyen, A. L., McDermott, K. B., Shimony, J. S., Snyder, A. Z., Schlaggar, B. L., Petersen, S. E., Nelson, S. M., & Dosenbach, N. U. F. (2017). Precision functional mapping of individual human brains. *Neuron*, *95*(4), 791–807.e7. https://doi.org/10.1016/j.neuron.2017.07.011

Goto, M., Abe, O., Miyati, T., Yamasue, H., Gomi, T., & Takeda, T. (2016). Head motion and correction methods in resting-state functional MRI. *Magnetic resonance in medical sciences: MRMS: An Official Journal of Japan Society of Magnetic Resonance in Medicine*, *15*(2), 178–186. https://doi.org/10.2463/mrms.rev.2015-0060

Gowland, P. A., & Bowtell, R. (2007). Theoretical optimization of multi-echo fMRI data acquisition. *Physics in Medicine & Biology*, *52*(7), 1801. https://doi.org/10.1088/0031-9155/52/7/003

Graham, M. S., Drobnjak, I., Jenkinson, M., & Zhang, H. (2017). Quantitative assessment of the susceptibility artefact and its interaction with motion in diffusion MRI. *PLoS One*, *12*(10), e0185647. https://doi.org/10.1371/journal.pone.0185647

Greene, D. J., Koller, J. M., Hampton, J. M., Wesevich, V., Van, A. N., Nguyen, A. L., Hoyt, C. R., McIntyre, L., Earl, E. A., Klein, R. L., Shimony, J. S., Petersen, S. E., Schlaggar, B. L., Fair, D. A., & Dosenbach, N. U. F. (2018). Behavioral interventions for reducing head motion during MRI scans in children. *NeuroImage*, *171*, 234–245. https://doi.org/10.1016/j.neuroimage.2018.01.023

Haskell, M. W., Nielsen, J.-F., & Noll, D. C. (2023). Off-resonance artifact correction for MRI: A review. *NMR in Biomedicine*, *36*(5), e4867. https://doi.org/10.1002/nbm.4867

Hausman, H. K., Hardcastle, C., Kraft, J. N., Evangelista, N. D., Boutzoukas, E. M., O'Shea, A., Albizu, A., Langer, K., Van Etten, E. J., Bharadwaj, P. K., Song, H., Smith, S. G., Porges, E., Hishaw, G. A., Wu, S., DeKosky, S., Alexander, G. E., Marsiske, M., Cohen, R., & Woods, A. J. (2022). The association between head motion during functional magnetic resonance imaging and executive functioning in older adults. *Neuroimage: Reports*, *2*(2), 100085. https://doi.org/10.1016/j.ynirp.2022.100085

Hermosillo, R. J. M., Moore, L. A., Feczko, E., Miranda-Domínguez, Ó., Pines, A., Dworetsky, A., Conan, G., Mooney, M. A., Randolph, A., Graham, A., Adeyemo, B., Earl, E., Perrone, A., Carrasco, C. M., Uriarte-Lopez, J., Snider, K., Doyle, O., Cordova, M., Koirala, S., … Fair, D. A. (2024). A precision functional atlas of personalized network topography and probabilities. *Nature Neuroscience*, *27*(5), 1000–1013. https://doi.org/10.1038/s41593-024-01596-5

Hollarek, M., van Buuren, M., Asscheman, J. S., Cillessen, A. H. N., Koot, S., van Lier, P. A. C., & Krabbendam, L. (2023). Predicting change in neural activity during social exclusion in late childhood: The role of past peer experiences. *Social Neuroscience*, *18*(2), 65–79. https://doi.org/10.1080/17470919.2023.2207837

Hutton, C., Andersson, J., Deichmann, R., & Weiskopf, N. (2013). Phase informed model for motion and susceptibility. *Human Brain Mapping*, *34*(11), 3086–3100. https://doi.org/10.1002/hbm.22126

Jernigan, T. L., Brown, S. A., & Dowling, G. J. (2018). The adolescent brain cognitive development study. *Journal of Research on Adolescence: The Official Journal of the Society for Research on Adolescence*, *28*(1), 154–156. https://doi.org/10.1111/jora.12374

Jezzard, P., & Balaban, R. S. (1995). Correction for geometric distortion in echo planar images from B0 field variations. *Magnetic Resonance in Medicine*, *34*(1), 65–73. https://doi.org/10.1002/mrm.1910340111

Kay, B. P., Wheelock, M. D., Siegel, J. S., Raut, R. V., Chauvin, R. J., Metoki, A., Rajesh, A., Eck, A., Pollaro, J., Wang, A., Suljic, V., Adeyemo, B., Baden, N. J., Scheidter, K. M., Monk, J., Ramirez-Perez, N., Krimmel, S. R., Shinohara, R. T., Tervo-Clemmens, B., … Dosenbach, N. U. F. (2025). Stimulant medications affect arousal and reward, not attention networks. *Cell*, *188*(26), 7529–7546.e20. https://doi.org/10.1016/j.cell.2025.11.039

Krimmel, S. R., Laumann, T. O., Chauvin, R. J., Hershey, T., Roland, J. L., Shimony, J. S., Willie, J. T., Norris, S. A., Marek, S., Van, A. N., Wang, A., Monk, J., Scheidter, K. M., Whiting, F. I., Ramirez-Perez, N., Metoki, A., Baden, N. J., Kay, B. P., Siegel, J. S., Nahman-Averbuch, H., … Dosenbach, N. U. F. (2025). The human brainstem's red nucleus was upgraded to support goal-directed action. *Nature Communications*, *16*(1), 3398. https://doi.org/10.1038/s41467-025-58172-z

Kundu, P., Brenowitz, N. D., Voon, V., Worbe, Y., Vértes, P. E., Inati, S. J., Saad, Z. S., Bandettini, P. A., & Bullmore, E. T. (2013). Integrated strategy for improving functional connectivity mapping using multiecho fMRI. *Proceedings of the National Academy of Sciences*, *110*(40), 16187–16192. https://doi.org/10.1073/pnas.1301725110

Kundu, P., Inati, S. J., Evans, J. W., Luh, W.-M., & Bandettini, P. A. (2012). Differentiating BOLD and non-BOLD signals in fMRI time series using multi-echo EPI. *NeuroImage*, *60*(3), 1759–1770. https://doi.org/10.1016/j.neuroimage.2011.12.028

Kundu, P., Voon, V., Balchandani, P., Lombardo, M. V., Poser, B. A., & Bandettini, P. A. (2017). Multi-echo fMRI: A review of applications in fMRI denoising and analysis of BOLD signals. *NeuroImage*, *154*, 59–80. https://doi.org/10.1016/j.neuroimage.2017.03.033

Laumann, T. O., Zorumski, C. F., & Dosenbach, N. U. (2023). Precision neuroimaging for localization-related psychiatry. *JAMA Psychiatry*, *80*(8), 763. https://doi.org/10.1001/jamapsychiatry.2023.1576

Lynch, C. J., Elbau, I. G., Ng, T., Ayaz, A., Zhu, S., Wolk, D., Manfredi, N., Johnson, M., Chang, M., Chou, J., Summerville, I., Ho, C., Lueckel, M., Bukhari, H., Buchanan, D., Victoria, L. W., Solomonov, N., Goldwaser, E., Moia, S., … Liston, C. (2024). Frontostriatal salience network expansion in individuals in depression. *Nature*, *633*(8030), 624–633. https://doi.org/10.1038/s41586-024-07805-2

Lynch, C. J., Elbau, I. G., Ng, T. H., Wolk, D., Zhu, S., Ayaz, A., Power, J. D., Zebley, B., Gunning, F. M., & Liston, C. (2022). Automated optimization of TMS coil placement for personalized functional network engagement. *Neuron*, *110*(20), 3263–3277.e4. https://doi.org/10.1016/j.neuron.2022.08.012

Lynch, C. J., Power, J. D., Scult, M. A., Dubin, M., Gunning, F. M., & Liston, C. (2020). Rapid precision functional mapping of individuals using multi-echo fMRI. *Cell Reports*, *33*(12), 108540. https://doi.org/10.1016/j.celrep.2020.108540

Makowski, C., Lepage, M., & Evans, A. C. (2019). Head motion: The dirty little secret of neuroimaging in psychiatry. *Journal of Psychiatry & Neuroscience: JPN*, *44*(1), 62–68. https://doi.org/10.1503/jpn.180022

Marcus, D., Harwell, J., Olsen, T., Hodge, M., Glasser, M., Prior, F., Jenkinson, M., Laumann, T., Curtiss, S. W., & Van Essen, D. (2011). Informatics and data mining tools and strategies for the human connectome project. *Frontiers in Neuroinformatics*, *5*, 4. https://doi.org/10.3389/fninf.2011.00004

Marek, S., Tervo-Clemmens, B., Calabro, F. J., Montez, D. F., Kay, B. P., Hatoum, A. S., Donohue, M. R., Foran, W., Miller, R. L., Hendrickson, T. J., Malone, S. M., Kandala, S., Feczko, E., Miranda-Dominguez, O., Graham, A. M., Earl, E. A., Perrone, A. J., Cordova, M., Doyle, O., … Dosenbach, N. U. F. (2022). Reproducible brain-wide association studies require thousands of individuals. *Nature*, *603*(7902), 654–660. https://doi.org/10.1038/s41586-022-04492-9

McCormick, M., Liu, X., Ibanez, L., Jomier, J., & Marion, C. (2014). ITK: Enabling reproducible research and open science. *Frontiers in Neuroinformatics*, *8*, 13. https://doi.org/10.3389/fninf.2014.00013

Montez, D. F., Van, A. N., Miller, R. L., Seider, N. A., Marek, S., Zheng, A., Newbold, D. J., Scheidter, K., Feczko, E., Perrone, A. J., Miranda-Dominguez, O., Earl, E. A., Kay, B. P., Jha, A. K., Sotiras, A., Laumann, T. O., Greene, D. J., Gordon, E. M., Tisdall, M. D., … Dosenbach, N. U. F. (2023). Using synthetic MR images for distortion correction. *Developmental Cognitive Neuroscience*, *60*, 101234. https://doi.org/10.1016/j.dcn.2023.101234

Newbold, D. J., & Dosenbach, N. U. (2021). Tracking plasticity of individual human brains. *Current Opinion in Behavioral Sciences*, *40*, 161–168. https://doi.org/10.1016/j.cobeha.2021.04.018

Newbold, D. J., Laumann, T. O., Hoyt, C. R., Hampton, J. M., Montez, D. F., Raut, R. V., Ortega, M., Mitra, A., Nielsen, A. N., Miller, D. B., Adeyemo, B., Nguyen, A. L., Scheidter, K. M., Tanenbaum, A. B., Van, A. N., Marek, S., Schlaggar, B. L., Carter, A. R., Greene, D. J., … Dosenbach, N. U. F. (2020). Plasticity and spontaneous activity pulses in disused human brain circuits. *Neuron*, *107*(3), 580–589.e6. https://doi.org/10.1016/j.neuron.2020.05.007

Port, J. D., & Pomper, M. G. (2000). Quantification and minimization of magnetic susceptibility artifacts on GRE images. *Journal of Computer Assisted Tomography*, *24*(6), 958–964. https://doi.org/10.1097/00004728-200011000-00024

Posse, S. (2012). Multi-echo acquisition. *NeuroImage*, *62*(2), 665–671. https://doi.org/10.1016/j.neuroimage.2011.10.057

Power, J. D., Barnes, K. A., Snyder, A. Z., Schlaggar, B. L., & Petersen, S. E. (2012). Spurious but systematic correlations in functional connectivity MRI networks arise from subject motion. *NeuroImage*, *59*(3), 2142–2154. https://doi.org/10.1016/j.neuroimage.2011.10.018

Power, J. D., Silver, B. M., Silverman, M. R., Ajodan, E. L., Bos, D. J., & Jones, R. M. (2019). Customized head molds reduce motion during resting state fMRI scans. *NeuroImage*, *189*, 141–149. https://doi.org/10.1016/j.neuroimage.2019.01.016

Saggar, M., Shine, J. M., Liégeois, R., Dosenbach, N. U. F., & Fair, D. (2022). Precision dynamical mapping using topological data analysis reveals a hub-like transition state at rest. *Nature Communications*, *13*(1), 4791. https://doi.org/10.1038/s41467-022-32381-2

Siegel, J. S., Subramanian, S., Perry, D., Kay, B. P., Gordon, E. M., Laumann, T. O., Reneau, T. R., Metcalf, N. V., Chacko, R. V., Gratton, C., Horan, C., Krimmel, S. R., Shimony, J. S., Schweiger, J. A., Wong, D. F., Bender, D. A., Scheidter, K. M., Whiting, F. I., Padawer-Curry, J. A., … Dosenbach, N. U. F. (2024). Psilocybin desynchronizes the human brain. *Nature*, *632*(8023), 131–138. https://doi.org/10.1038/s41586-024-07624-5

Smith, S. M., Jenkinson, M., Woolrich, M. W., Beckmann, C. F., Behrens, T. E. J., Johansen-Berg, H., Bannister, P. R., De Luca, M., Drobnjak, I., Flitney, D. E., Niazy, R. K., Saunders, J., Vickers, J., Zhang, Y., De Stefano, N., Brady, J. M., & Matthews, P. M. (2004). Advances in functional and structural MR image analysis and implementation as FSL. *NeuroImage*, *23*, S208–S219. https://doi.org/10.1016/j.neuroimage.2004.07.051

Togo, H., Rokicki, J., Yoshinaga, K., Hisatsune, T., Matsuda, H., Haga, N., & Hanakawa, T. (2017). Effects of field-map distortion correction on resting state functional connectivity MRI. *Frontiers in Neuroscience*, *11*, 656. https://doi.org/10.3389/fnins.2017.00656

Visser, E., Poser, B. A., Barth, M., & Zwiers, M. P. (2012). Reference-free unwarping of EPI data using dynamic off-resonance correction with multiecho acquisition (DOCMA). *Magnetic Resonance in Medicine*, *68*(4), 1247–1254. https://doi.org/10.1002/mrm.24119

Weiskopf, N., Klose, U., Birbaumer, N., & Mathiak, K. (2005). Single-shot compensation of image distortions and BOLD contrast optimization using multi-echo EPI for real-time fMRI. *NeuroImage*, *24*(4), 1068–1079. https://doi.org/10.1016/j.neuroimage.2004.10.012

Wilm, B. J., Barmet, C., Pavan, M., & Pruessmann, K. P. (2011). Higher order reconstruction for MRI in the presence of spatiotemporal field perturbations. *Magnetic Resonance in Medicine*, *65*(6), 1690–1701. https://doi.org/10.1002/mrm.22767

Zheng, A., Montez, D. F., Marek, S., Gilmore, A. W., Newbold, D. J., Laumann, T. O., Kay, B. P., Seider, N. A., Van, A. N., Hampton, J. M., Alexopoulos, D., Schlaggar, B. L., Sylvester, C. M., Greene, D. J., Shimony, J. S., Nelson, S. M., Wig, G. S., Gratton, C., McDermott, K. B., Raichle, M. E., Gordon, E. M., & Dosenbach, N. U. F. (2021). Parallel hippocampal-parietal circuits for self- and goal-oriented processing. *Proceedings of the National Academy of Sciences*, *118*(34), e2101743118. https://doi.org/10.1073/pnas.2101743118